The Homogeneity of Optimal Sensor Placement Across Multiple Winged Insect Species

Abigail L. Jenkins

A thesis
submitted in partial fulfillment of the
requirements for the degree of

Master of Science

University of Washington

2016

Committee:

Kristi Morgansen Hill, Chair

Thomas Daniel

Program Authorized to Offer Degree:
Aeronautics and Astronautics

University of Washington

Abstract

The Homogeneity of Optimal Sensor Placement Across Multiple Winged Insect Species

Abigail L. Jenkins

Chair of the Supervisory Committee:
Associate Professor Kristi Morgansen Hill
Aeronautics and Astronautics

Taking inspiration from biology, control algorithms can be implemented to imitate the naturally occurring control systems present in nature. This research is primarily concerned with insect flight and optimal wing sensor placement. Many winged insects with halteres are equipped with mechanoreceptors termed campaniform sensilla. Although the exact information these receptors provide to the insect's nervous system is unknown, it is thought to have the capability of measuring inertial rotation forces. During flight, when the wing bends, the information measured by the campaniform sensilla is received by the central nervous system, and provides the insect necessary data to control flight. This research compares three insect species - the hawkmoth *Manduca sexta*, the honeybee *Apis mellifera*, and the fruit fly *Drosophila melanogaster*. Using an observability-based sensor placement algorithm, the optimal sensor placement for these three species is determined. Simulations resolve if this optimal sensor placement corresponds to the insect's campaniform sensilla, as well as if placement is homogeneous across species.

TABLE OF CONTENTS

LIST OF FIGURES

LIST OF TABLES

ACKNOWLEDGMENTS

This thesis represents a year of research during my time at the University of Washington. I would like to thank my advisor, Kristi Morgansen, who helped guide my research ideas and motivated me when life was doing otherwise. Tom Daniel and his student, Annika Eberle, were valuable resources and were able to steer me in useful directions based on their own lessons learned. This work was supported in part by Air Force Office of Scientific Research grant number FA9550-11-1-0155 MODP06.

I would like to thank my parents and two brothers, who cultivated my interest in engineering and are continuously supportive. Finally, I would like to thank my boyfriend, Tyler Shea, for supporting me and providing a shoulder to lean on when the going got rough.

DEDICATION

to my parents, Scott and Lorie Jenkins, and my boyfriend, Tyler Shea

Chapter 1

INTRODUCTION

An important limiting factor in most control systems is the reliance on the capability and functionality of the sensors present in the system. High fidelity sensors are expensive, and in a limited sensing environment it becomes necessary to develop technology which can operate robustly with an undersensed system. In an undersensed system there are not enough sensors on board to measure the complete state of the vehicle. However, using control and observability theory, it is possible to sense the full state by purposefully actuating the system. Sensors can be placed strategically so that when the system is actuated, the sensors are able to create a complete picture of the vehicle.

A part of controlling any given system requires having the correct number and type of sensor to provide the system with necessary data. This data can be used to feed back into the system. It is important to provide enough information with limited sensors to accurately control the system. With limited sensors, it is imperative to determine the sensor locations which will provide the most information. Many mechanical systems have a small number of expensive sensors which provide many types of information. By taking inspiration from biology, we can look at distributed sensors. This allows for very simple sensors, which, placed in specific locations, can give enough information about the system to provide control. An example of this distributed system in nature is seen in winged insects. Through analysis of the wing anatomy and wing stroke kinematics of an insect wing, a model can be created to determine wing vibration frequencies and shapes. From this, the wing information and results from the mode

shape, the optimal placement for a desired number of sensors can be determined. An analysis of optimal sensor placement for multiple insect species can answer the questions: does this optimal placement correspond to the campaniform sensilla present in the insect wings? Is this optimal placement homogeneous among winged insect species?

1.1 Literature Review

A review of wing stroke kinematics and structural properties was performed using [3, 1, 4, 5]. Prior research using optimal sensor placement in [2] was reviewed to determine methods used in wing flapping simulations and convex optimization. Finally, free vibration analysis methods in [6] were used to analyze spatial mode shapes of insect wings.

1.2 Contributions of this Thesis

This thesis addresses the question of whether optimal sensor placement on insect wings is homogeneous throughout three different types of insect species. It also addresses how sensor placement changes when we assume different structural mode shapes to describe the wing motion. There are many techniques to develop mode shapes, and it is important to determine which of these produces more accurate results. This thesis determined that spatial mode shapes, specifically torsion modes, greatly impact optimized sensor results. Wing shape was found to alter the sensor placement, with the hawkmoth and fruit fly resulting in similar structure of optimized sensors. Additionally, it determined that optimizing for strain does not correspond to campaniform sensilla structure in the hawkmoth and fruit fly, implying that campaniform sensilla may be sensing information other than strain.

1.3 Organization of the Report

The organization of this report is the following. First, the flapping dynamics of the three insect wings are derived in Chapter 2. Then, FEA models of the wings are discussed in Chapter 3. In Chapter 4, the simulation of the flapping wings is reviewed. Chapter 5 discusses the results for each insect species and gives a brief summary, and finally in Chapter 6 further work is suggested.

Chapter 2
FLAPPING DYNAMICS

The flapping dynamics of the insect wings to be used in the work here was originally derived in [2] and will be shown here for completeness. In the model, the wings were assumed to resemble a thin flexible plate with the second-order nonlinear differential model described below. Additionally, the wing stroke kinematics are discussed. Aerodynamic forces and observability measures are described in [2]. The observability measures described provide the basis for the optimization of sensor placement.

2.1 Structural Dynamics

The structural dynamics of the wing are derived using a thin plate approximation. In order to develop the optimal sensor placement, the motion of the wing is required to determine the locations which would provide the most information. The out of plane motion of the wing can be described as

$$w(x, y, t) = \sum_{i=1}^{n} \phi_i(x, y)\eta_i(t) \tag{2.1}$$

where n is the number of mode shapes, ϕ are the functional representation of the spatial mode shapes, and η are the time-based modal coordinates. These mode shapes are described in Chapter 3, where an Ansys free vibration analysis determined the first bending and torsion mode shapes for each of the species considered. Additionally, these mode shapes can be used to describe the position of a small element on the wing, given by

$$\mathbf{r}(x, y, t) = x\hat{\mathbf{i}}_\mathbf{p} + y\hat{\mathbf{j}}_\mathbf{p} + w(x, y, t)\hat{\mathbf{k}}_\mathbf{p}. \tag{2.2}$$

The velocity of the position of an element is given by the derivative of (2.2):

$$\mathbf{v} = \mathbf{v_0} + \frac{\partial}{\partial t}\mathbf{r} + \omega_o \times \mathbf{r}. \tag{2.3}$$

Let the velocity of the plate coordinate system be given by

$$\mathbf{v_0} = U\hat{\mathbf{i}}_\mathbf{p} + V\hat{\mathbf{j}}_\mathbf{p} + W\hat{\mathbf{k}}_\mathbf{p} \tag{2.4}$$

and the angular velocity of the plate coordinate system be given as

$$\omega_0 = P\hat{\mathbf{i}}_\mathbf{p} + Q\hat{\mathbf{j}}_\mathbf{p} + R\hat{\mathbf{k}}_\mathbf{p}. \tag{2.5}$$

The velocity can then be written as

$$\begin{aligned}\mathbf{v} =& U\hat{\mathbf{i}}_\mathbf{p} + V\hat{\mathbf{j}}_\mathbf{p} + W\hat{\mathbf{k}}_\mathbf{p} + \dot{\omega}\hat{\mathbf{k}}_\mathbf{p} + (Qw - Ry)\hat{\mathbf{i}}_\mathbf{p} - (Pw - Rx)\hat{\mathbf{j}}_\mathbf{p} \\ &+ (Py - Qx)\hat{\mathbf{k}}_\mathbf{p}\end{aligned} \tag{2.6}$$

which can be simplified to

$$\mathbf{v} = (U + Qw - Ry)\hat{\mathbf{i}}_\mathbf{p} + (V + Rx - Pw)\hat{\mathbf{j}}_\mathbf{p} + (W + \dot{\omega} + Py - Qx)\hat{\mathbf{k}}_\mathbf{p}. \tag{2.7}$$

Next, let us define density as $\rho(x, y)$ and wing thickness as $h(x, y)$. The kinetic energy of the wing is defined by

$$T_e(t) = \frac{1}{2}\int_{\mathcal{A}} \rho(x, y)h(x, y)\mathbf{v}(x, y, t) \cdot \mathbf{v}(x, y, t)\mathrm{d}\mathcal{A}. \tag{2.8}$$

The potential energy can be determined by first defining the strain vector as

$$\chi = \begin{bmatrix} \partial^2 w/\partial x^2 \\ \partial^2 w/\partial y^2 \\ 2\partial^2 w/\partial x \partial y \end{bmatrix} \tag{2.9}$$

and subsequently defining the potential energy as

$$U_e(t) = \frac{1}{2} \int_{\mathcal{A}} \frac{h(x,y)^3}{12} \chi(x,y,t)^T D \chi(x,y,t) \mathrm{d}\mathcal{A} \tag{2.10}$$

where D is the matrix of material constants of the wing. Next, we can use Lagrange's equations to give

$$\frac{\mathrm{d}}{\mathrm{d}t}\left(\frac{\partial T_e}{\partial \dot{\eta}_i}\right) - \frac{\partial T_e}{\partial \eta_i} + \frac{\partial U_e}{\partial \eta_i} = \mathbf{Q_i}, \ i = 1, \ldots, n \tag{2.11}$$

where $\mathbf{Q}$ are the exogenous non-conservative generalized forces. The kinetic energy is expanded as

$$\begin{aligned} T_e(t) = & \frac{1}{2} \int_{\mathcal{A}} \rho h \left[(U + Qw - Ry)^2 + (V + Rx - Pw)^2 \right. \\ & \left. + (\omega + \dot{\omega} + Py - Qx)^2 \right] \mathrm{d}\mathcal{A}. \end{aligned} \tag{2.12}$$

Taking the partial derivative with respect to $\dot{\eta}_i$, we have

$$\frac{\partial T_e}{\partial \dot{\eta}_i} = \int_{\mathcal{A}} \rho h (W + \sum_{j=1} n \phi_j \dot{\eta}_j + Py - Qx) \phi_i \mathrm{d}\mathcal{A}. \tag{2.13}$$

Finally, the first term in Equation (2.11) is given by

$$\frac{\mathrm{d}}{\mathrm{d}t}\left(\frac{\partial T_e}{\partial \dot{\eta}_i}\right) = \int_{\mathcal{A}} \rho h \phi_i \left(\dot{W} + \dot{P}y - \dot{Q}x + \sum_{j=1}^{n} \phi_j \ddot{\eta}_j \right) \mathrm{d}\mathcal{A}. \tag{2.14}$$

Given the orthonormality of the mode shapes, we can simplify the first term to

$$\frac{\mathrm{d}}{\mathrm{d}t}\left(\frac{\partial T_e}{\partial \dot{\eta}}\right) = \ddot{\eta} + M_a \begin{bmatrix} \dot{W} \\ \dot{P} \\ \dot{Q} \end{bmatrix} \tag{2.15}$$

where M_a is the mass matrix, defined as

$$M_{a_i} = \int_{\mathcal{A}} \begin{bmatrix} \rho h \phi_i & \rho h \phi_i y & -\rho h \phi_i x \end{bmatrix} \mathrm{d}\mathcal{A}. \tag{2.16}$$

The second term can be written as

$$\begin{aligned} \frac{\partial T_e}{\partial \eta_i} = \int_{\mathcal{A}} \rho h \Bigg[& (U - Ry + Q\sum_{j=1}^{n} \phi_j \eta_j) Q\phi_i - (V + Rx \\ & - P\sum_{j=1}^{n} \phi_j \eta_j) P\phi_i \Bigg] \mathrm{d}\mathcal{A}. \end{aligned} \tag{2.17}$$

This can then be rewritten as

$$\frac{\partial T_e}{\partial \eta_n} = (Q^2 + P^2)\eta + M_a C_a(\mathbf{v_0}, \omega_0) \tag{2.18}$$

where C_a is the Coriolis force given by

$$C_a(\mathbf{v_0}, \omega_0) = \begin{bmatrix} QU - PV \\ -QR \\ PR \end{bmatrix}. \tag{2.19}$$

The third term can be written as

$$\frac{\partial U_e}{\partial \eta_i} = \int_{\mathcal{A}} = \frac{h^3}{12} \left(\frac{\partial \chi}{\partial \eta_i}\right)^T D\chi \mathrm{d}\mathcal{A} = \Omega\eta \tag{2.20}$$

where Ω is the diagonal modal frequency matrix. Finally, the dynamics are written

as

$$\ddot{\eta} + (\Omega - Q^2 - P^2)\eta + M_a \left(\begin{bmatrix} \dot{W} \\ \dot{P} \\ \dot{Q} \end{bmatrix} - \begin{bmatrix} QU - PV \\ -QR \\ PR \end{bmatrix} \right) = \mathbf{Q}. \tag{2.21}$$

2.2 Wing Stroke Kinematics

The flapping of the wings can be described using three angles: ϕ, θ, and α. These terms describe the position, elevation, and feathering angle, respectively, and are shown in Figure 2.1.

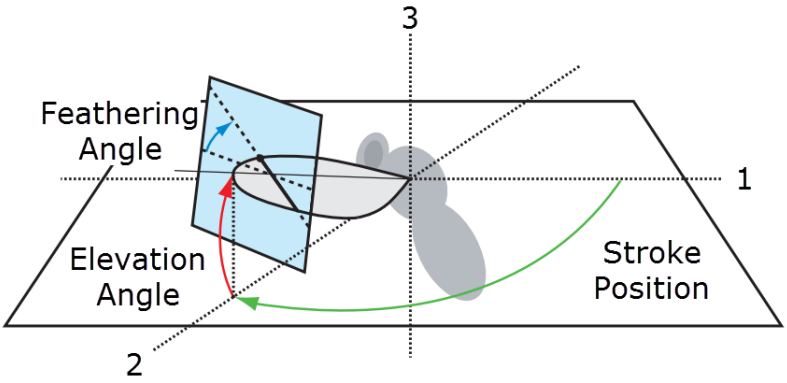

Figure 2.1: Wing stroke kinematics. Stroke position is represented by ϕ, elevation angle by θ, and feathering angle by α. [1]

In order to accurately model the wing kinematics, we must convert from inertial frame coordinates to wing reference frame. The coordinate system transformation is accomplished through a 3-1-2 Euler rotation sequence, where the axes are as shown in Figure 2.1. First, the reference frame is rotated around the 3-axis by the position angle ϕ, which is given by

$$R_3(\phi) = \begin{bmatrix} \cos\phi & \sin\phi & 0 \\ -\sin\phi & \cos\phi & 0 \\ 0 & 0 & 1 \end{bmatrix}. \tag{2.22}$$

Second, the frame is rotated around the 1-axis by the elevation angle,

$$R_1(\theta) = \begin{bmatrix} 1 & 0 & 0 \\ 0 & \cos\theta & \sin\theta \\ 0 & -\sin\theta & \cos\theta \end{bmatrix}, \tag{2.23}$$

and finally the frame is rotated around the 2-axis by the feathering angle, given by

$$R_2(\alpha) = \begin{bmatrix} \cos\alpha & 0 & \sin\alpha \\ 0 & 1 & 0 \\ \sin\alpha & 0 & \cos\alpha \end{bmatrix}. \tag{2.24}$$

These three rotations result in the rotation matrix

$$R(\phi, \alpha, \theta) = R_2(\alpha)R_1(\theta)R_3(\phi) \tag{2.25}$$

which transforms the inertial frame to the wing frame. It is then necessary to derive the inverse and forward kinematics. Let the Euler angles be defined as

$$\mathbf{u} = \begin{bmatrix} \theta \\ \alpha \\ \phi \end{bmatrix} \tag{2.26}$$

and the wing axis angular rates as

$$\omega_0 = \begin{bmatrix} P \\ Q \\ R \end{bmatrix}. \tag{2.27}$$

Additionally, the unit vectors in each direction are given by $\hat{\mathbf{e}}_\mathbf{1}$, $\hat{\mathbf{e}}_\mathbf{2}$, and $\hat{\mathbf{e}}_\mathbf{3}$. The inverse kinematics are then given by

$$\omega_0 = \begin{bmatrix} R_2(\alpha)\hat{\mathbf{e}}_\mathbf{1} & \hat{\mathbf{e}}_\mathbf{2} & R_2(\alpha)R_1(\theta)\hat{\mathbf{e}}_\mathbf{3} \end{bmatrix} \dot{\mathbf{u}}, \tag{2.28}$$

which is simplified to

$$\omega_0 = \begin{bmatrix} \cos\alpha & 0 & -\sin\alpha\cos\theta \\ 0 & 1 & \sin\theta \\ \sin\alpha & 0 & \cos\alpha\cos\theta \end{bmatrix} \begin{bmatrix} \dot{\theta} \\ \dot{\alpha} \\ \dot{\phi} \end{bmatrix}. \tag{2.29}$$

Using the inverse kinematics, we can invert the relationship to give the forward dynamics. This is accomplished by inverting the rotation matrix, which results in the forward dynamics given by

$$\begin{bmatrix} \dot{\theta} \\ \dot{\alpha} \\ \dot{\phi} \end{bmatrix} = \frac{1}{\cos\theta} \begin{bmatrix} \cos\alpha\cos\theta & 0 & \sin\alpha\cos\theta \\ \sin\alpha\sin\theta & \cos\theta & -\cos\alpha\sin\theta \\ -\sin\alpha & 0 & \cos\alpha \end{bmatrix} \omega_0. \tag{2.30}$$

Since the wing is not expected to reach large elevation angle, the singularity from a 3-1-2 rotation at $\theta = \pm\pi/2$ is not a problem for the purpose of these simulations.

Chapter 3

FINITE ELEMENT ANALYSIS MODELING

In order to simulate a flapping wing, it is necessary to determine the mode shapes and frequencies of each wing. This can be accomplished in a number of ways. As in previous research, a thin plate approximation can be used. However, this does not take into account the curvature and shape of the actual wing. In comparison, a finite element analysis (FEA) approach provides greater accuracy. Within the FEA approach, it is possible to attain differing levels of fidelity by altering the accuracy of the model. This can be accomplished mainly by taking into account non-homogeneous thickness and modeling the veination in the wing.

3.1 Prior Model

Previous research [2] used a cantilever thin plate approximation in order to determine the mode shapes for the hawkmoth *Manduca sexta*. From this theory, the first bending and torsion modes are shown in Figure 3.1. Each mode shape has been scaled to a maximum of unit deflection for easier viewing.

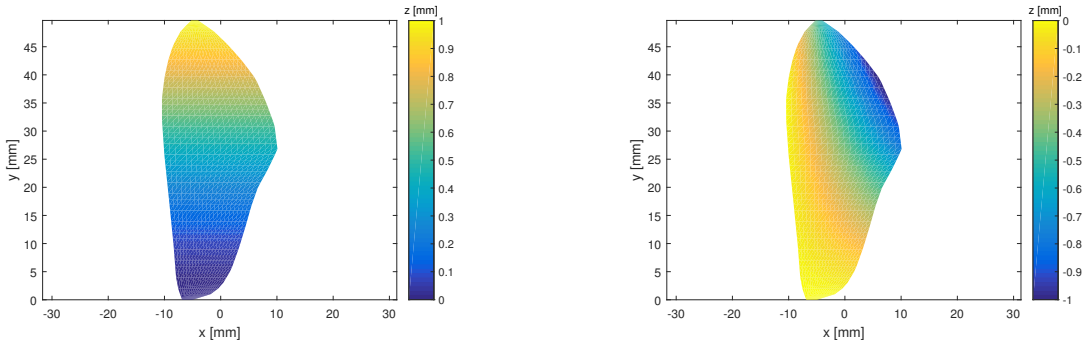

(a) First bending mode

(b) First torsion mode

Figure 3.1: Cantilever thin plate approximation.

This approach led to well defined mode shapes, and the sensor placement results are compared to those using an FEA approach in Chapter 6.

3.2 FEA Approach

In order to provide more accurate mode shapes than from prior research, a finite element analysis (FEA) approach was utilized. Specifically, Ansys FEA software was chosen. Additional FEA softwares, COMSOL and Abaqus, were considered, however the author had previous experience with Ansys. An FEA approach was chosen in order to include the true geometry of each wing shape in the mode shape analysis. This was assumed to provide more accurate results compared to a cantilever thin plate. Along with having the ability to represent the true wing shape, this made it possible to fix the wing at the root of the wing, compared to the entire end of a cantilever plate. When modeling the wings, multiple avenues were considered. However, a simple FEA model which used a wireframe of the wing for each species, a uniform thickness, and uniform material was chosen. Further research into creating higher fidelity models will be explored in Chapter 6.

3.2.1 Theory

In order to produce more accurate mode shapes for the three insects, the finite element software ANSYS was utilized. Using finite element analysis, the mode vibration shapes and frequencies can be determined by solving the equation of motion for a structure, given by

$$\Big[M\Big]\Big\{\ddot{u}\Big\} + \Big[C\Big]\Big\{\dot{u}\Big\} + \Big[K\Big]\Big\{u\Big\} = \Big\{F\Big\} \tag{3.1}$$

where $[M]$ is the mass matrix, $[C]$ is the damping matrix, $[K]$ is the stiffness matrix, $[F]$ is the force vector, and $u, \dot{u}, \ddot{u}$ are the displacement, velocity, and acceleration, respectively, of the structure. In order to find the free vibration modes, we assume there is no damping and no force vector. Therefore, we must solve the resulting equation

$$\Big[M\Big]\Big\{\ddot{u}\Big\} + \Big[K\Big]\Big\{u\Big\} = 0. \tag{3.2}$$

The results from solving Equation (3.2) will give the natural frequencies and the undamped mode shapes of the structure. The natural frequencies are the eigenvalues of the system while the mode shapes are the eigenvectors [6]. The mode shapes represent how the structure will deform under certain initial conditions.

For each insect wing, the root of the wing was fixed in all degrees of freedom, and all other nodes were fixed in x and y. This was to ensure only out of plane bending in the z direction.

It should be noted that the mode shapes found using ANSYS, or any finite element method, will result in a general shape of the wing. The amplitude of this shape will vary depending on initial conditions and forces on the structure. It can be alarming at first to see deflection magnitudes larger than the wing length, however it is important

to remember that the relative deflection between nodes is the important information and the shape can and must be scaled.

In the simulation algorithm, the modal shapes are scaled for unit modal mass, described by

$$\phi_n = \frac{\left[\phi\right]}{\sqrt{m}}. \tag{3.3}$$

In Equation (3.3), m is the total mass of the wing, defined by

$$m = \sum_{i=1}^{N}\sum_{j=1}^{M} \rho_{ij} h_{ij} \phi_{ij}^2 A_{ij} \tag{3.4}$$

where ρ is the wing density, h is the wing thickness, and A is the wing area.

3.2.2 Modeling

A wireframe of each insect wing was made from data on each insect species, and imported into Ansys. Using SHELL181 elements, each model was tested to ensure correctness of the model. A transverse force was applied at the free end of the wing (the forces were scaled for each wing length), and a static analysis was performed. The deflection of each simulation was analyzed to determine if the results were reasonable. Once each model was verified, a modal analysis was performed. The same model that was used for the transverse force analysis was utilized, with the transverse load removed. In order to perform a free vibration analysis, the only forces required are those which fix the model (e.g. each insect wing was fixed at the root to simulate how the wing moves relative to the insect body). The first five modes were extracted. Since the first bending and first torsion mode describe the bulk of a structure's dynamic properties as described in [2], these were the only two mode shapes chosen for the simulation. Wing structural properties were taken from [3].

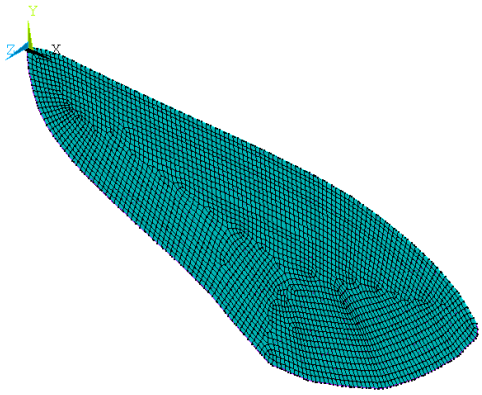

Figure 3.2: Hawkmoth FEA model, showing the shape of the model and the mesh used.

For each of the three species models, a mesh was used to create distinct spatial nodes. The mesh size varied between models, with the largest mesh used for the hawkmoth and the smallest for the drosophila. This was done to have approximately the same number of nodes for each wing. Figure 3.2 shows the Ansys model of the hawkmoth wing with the mesh. The three insect wing models are shown below in Figure 3.3.

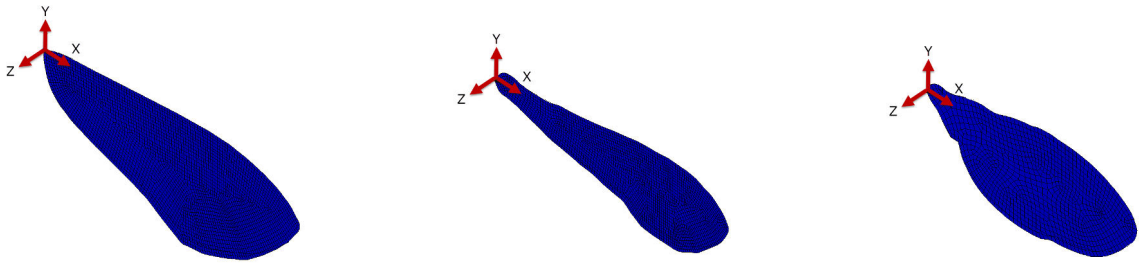

(a) (b) (c)

Figure 3.3: ANSYS models of the three insect wings, where (a) is the hawkmoth, (b) is the honeybee, and (c) is the fruit fly.

The results from ANSYS typically scale the results for unit modal mass. The figures

below show the mode shapes for the three different insects scaled for unit deflection. All three models produced very similar mode shapes, shown below in Figures 3.4, 3.5, and 3.6. The mode shape analyses produced similar results, with slight differences mainly in the torsion mode. These differences were due to the different wing shapes - the maximum deflection is seen on each wing at the most positive x location of the trailing edge.

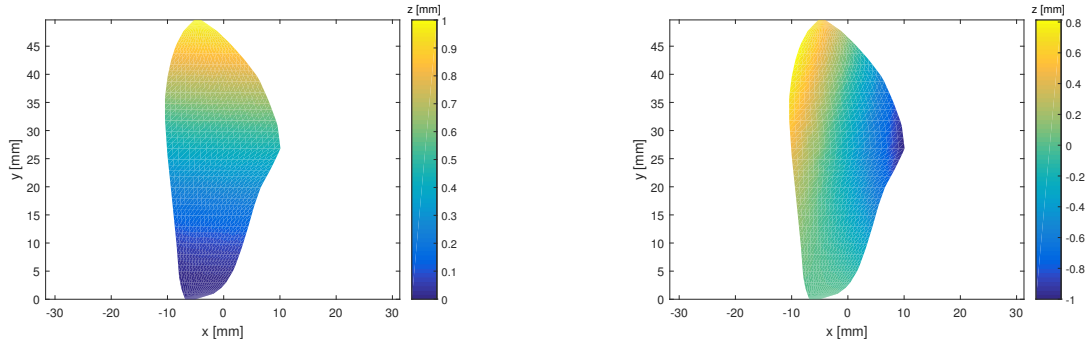

(a) First bending mode (b) First torsion mode

Figure 3.4: Hawkmoth modal shapes using Ansys FEA software.

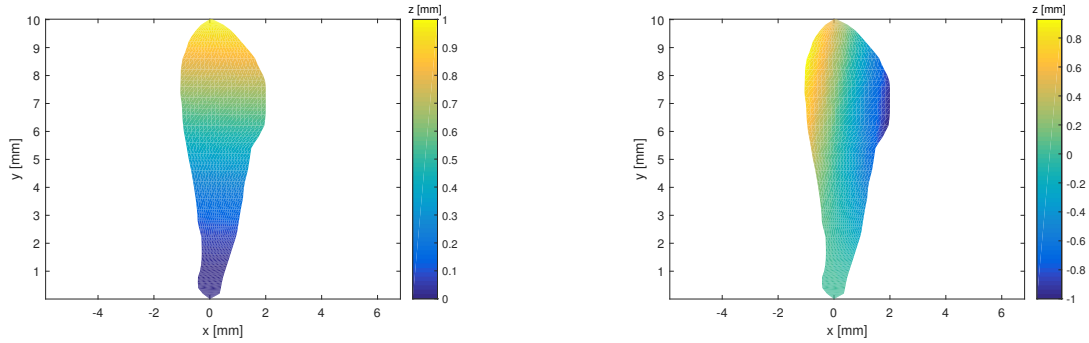

(a) First bending mode (b) First torsion mode

Figure 3.5: Honeybee modal shapes using Ansys FEA software.

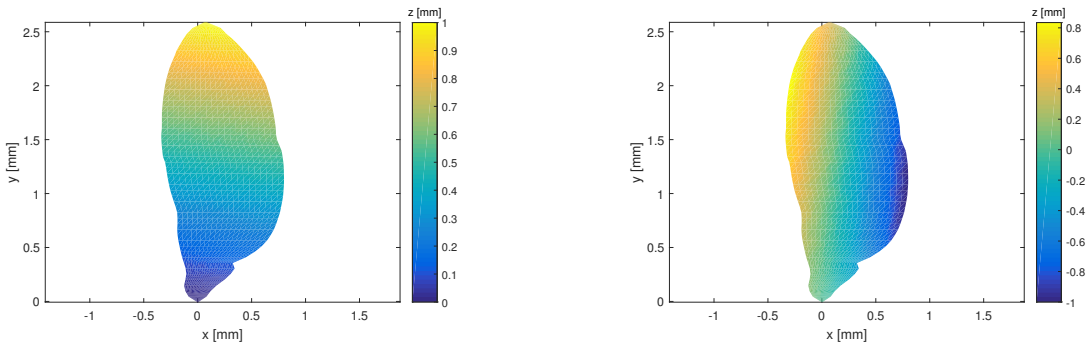

(a) First bending mode

(b) First torsion mode

Figure 3.6: Fruit fly modal shapes using Ansys FEA software.

3.3 Thin Plate vs. FEA Comparison

As shown in Figures 3.1 and 3.4, the bending mode using the thin plate approximation is very similar to the mode shape produced using Ansys. Comparing the two methods for the first bending mode produces almost identical results. However, a large disparity is seen in the torsion mode. The thin plate approximation produces a shape which twists around the leading edge, where Ansys produces results which show the wing twisting around a chord spanning from root to tip and has both positive and negative deflection. This difference is not trivial, and it will be elaborated on further in the results section.

Chapter 4

SIMULATION

4.1 Hawkmoth Parameters

The hawkmoth stroke kinematics were determined from animal studies and were used in [2], given by

$$\phi = -a_\phi \cos\left(\frac{2\pi t}{T}\right) \tag{4.1a}$$

$$\alpha = \frac{\pi}{2} - a_\alpha \tanh\left(\frac{\pi}{2}\sin\left(\frac{2\pi t}{T}\right)\right) \tag{4.1b}$$

$$\theta = 0 \tag{4.1c}$$

where a_ϕ and a_α are the stroke position amplitude and the feathering angle amplitude, respectively. The stroke angles are shown in Figure 4.1. The angles are stroke normalized, which means the data in Figure 4.1 represent a single wing beat. Along with the stroke angles, and mode shapes and planform described in Chapter 3, it is necessary to determine mode shape frequencies and damping ratios. The natural frequencies were found using the FEA analysis, then the frequencies were fine tuned, and damping ratios were chosen to resemble wing deflection as seen in [2]. The frequencies and damping ratios are shown below in Table 4.1.

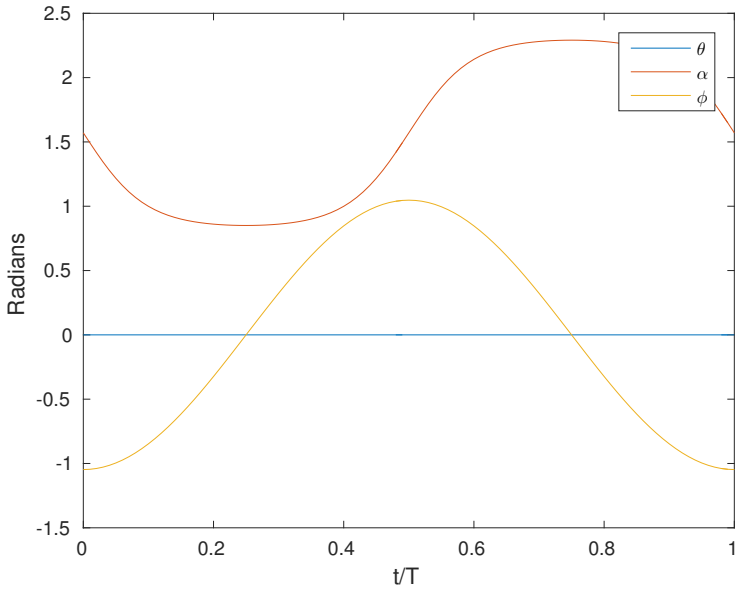

Figure 4.1: Wing stroke kinematics for the hawkmoth *Manduca sexta*.

4.2 Drosophila Parameters

The wing stroke kinematics of the Drosophila were those used in [5], given by

$$\phi = -\left[\frac{a_\phi}{\sin^{-1}(k_\phi)}\right] \sin^{-1}\left(k_\phi \cos\left(\frac{2\pi f t}{T}\right)\right) \tag{4.2a}$$

$$\alpha = \frac{\pi}{2} - \left[\frac{a_\alpha}{\tanh(k_\alpha)}\right] \tanh\left(k_\alpha \sin\left(\frac{2\pi f t}{T}\right)\right) \tag{4.2b}$$

$$\theta = 0 \tag{4.2c}$$

where a_ϕ and a_α are the stroke amplitude and feathering amplitude, respectively, and k_ϕ and k_α control the overall shape of the wing kinematics. Figure 4.2 shows the stroke kinematics, which resemble closely those used for the hawkmoth in Figure 4.1.

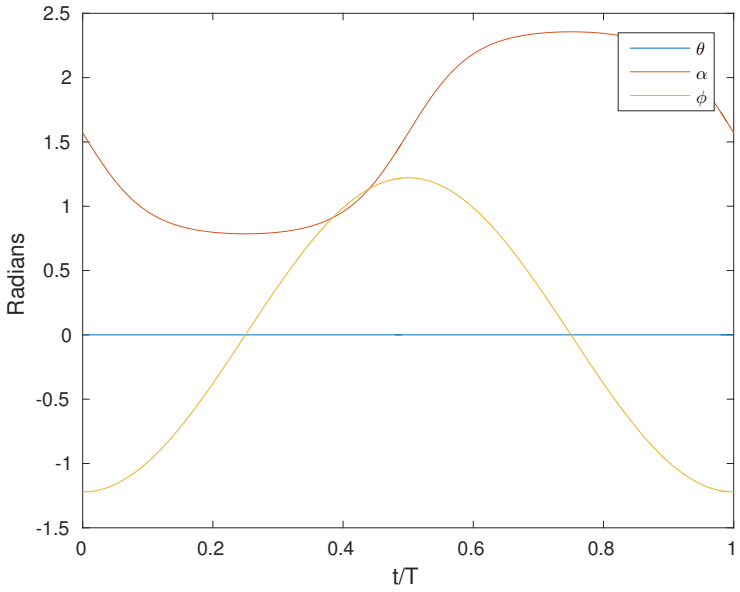

Figure 4.2: Wing stroke kinematics for the fruit fly *Drosophila melanogaster*.

4.3 Honeybee Parameters

The honeybee stroke kinematics were used from [4]. The data was found by recording the honeybee's wingstrokes, and was then averaged and stroke-normalized for smoother data. As shown below in Figure 4.3, the measured data can be approximated by the model used for the drosophila. In order to limit differences in the model to look at optimal sensor placement based mainly on wing shape, the approximation using Equation (4.2) was chosen. Further research into wing stroke differences will be explored in Chapter 6.

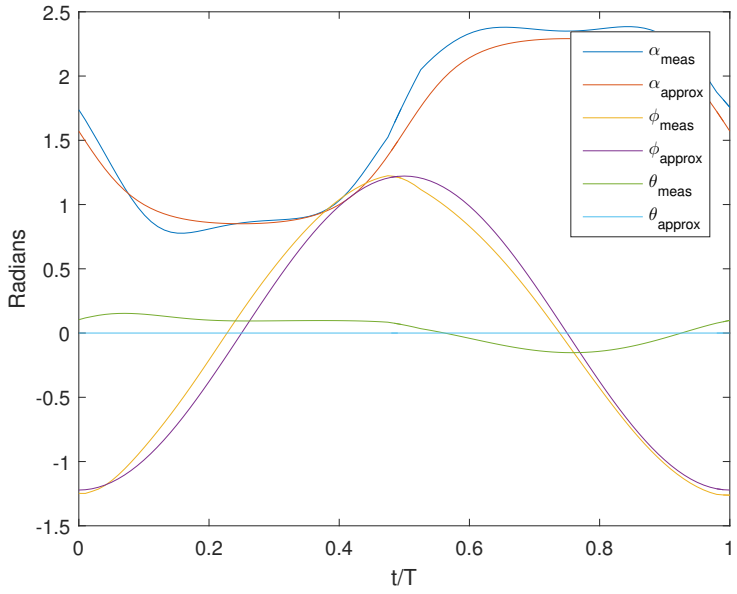

Figure 4.3: Wing stroke kinematics for the honeybee *Apis mellifera*.

The mode frequencies and damping ratios for each wing are shown below in Table 4.1.

Table 4.1: Mode frequencies and damping ratios for the hawkmoth, honeybee, and fruit fly.

	$\omega_{n,bending}$	$\omega_{n,torsion}$	$\zeta_{bending}$	$\zeta_{torsion}$
Hawkmoth	96	100	0.001	0.005
Fruit Fly	90	150	0.001	0.001
Honeybee	90	110	0.001	0.002

Chapter 5

RESULTS AND DISCUSSION

5.1 Sensor Placement Results

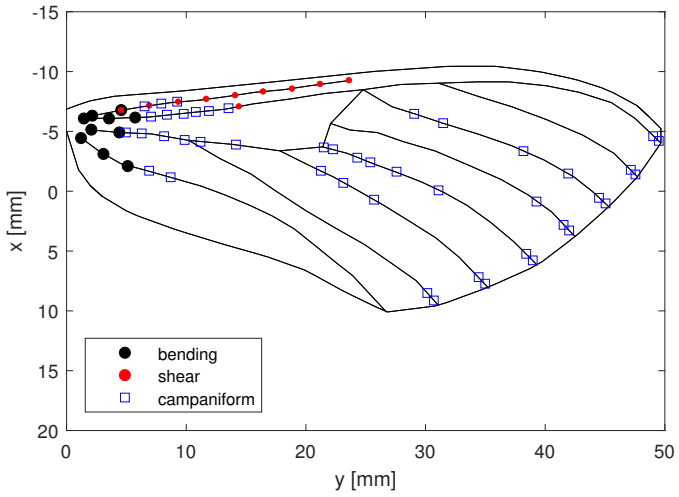

Figure 5.1: Optimal sensor placement for the hawkmoth *Manduca sexta*.

The optimal sensor placement analysis was similar to that used in [2], with minor changes. Prior research used a single optimization with a total number of 20 sensors. However, due to the differences in mode shapes between [2] and this study the results in this thesis show that certain bending and shear sensors share common nodes. Therefore, two optimizations were performed - one optimizing for 10 bending sensors, and a second optimizing for 10 shear sensors. The bending and shear optimizations were performed using Matlab's cvx convex optimization toolbox for all

three insect wings. The results for the hawkmoth *Manduca sexta*, fruit fly *Drosophila melanogaster*, and honeybee *Apis mellifera* are shown in Figures 5.1, 5.2, and 5.3, respectively.

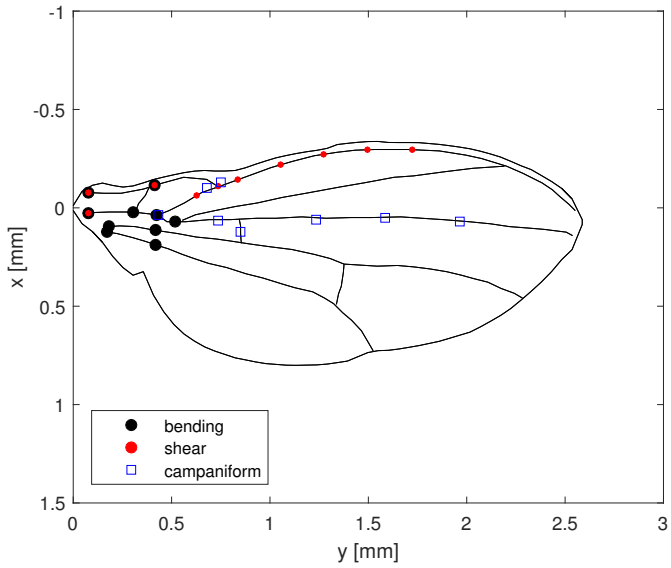

Figure 5.2: Optimal sensor placement for the fruit fly *Drosophila melanogaster*.

The hawkmoth and fruit fly wing shapes have similar aspect ratios and overall shape, which led to very similar sensor placement. The bending sensors were bundled near the root of the wing, similar to the results in [2]. The shear sensors using the FEA approach for the mode shapes produced different results than prior research, spanning from the root of the wing along the leading edge towards the tip of the wing. Based on the torsion mode shape, the most shear strain information lies along the leading and trailing edge of the wing. Therefore, the shear sensor results are as expected given the mode shape analysis. The honeybee optimizations resulted in drastic differences in sensor placement. This can be attributed to the wing shape having a narrow root and wide tip. The bending sensors are bundled near the root towards the trailing edge, while the shear sensors are bundled closest to the root.

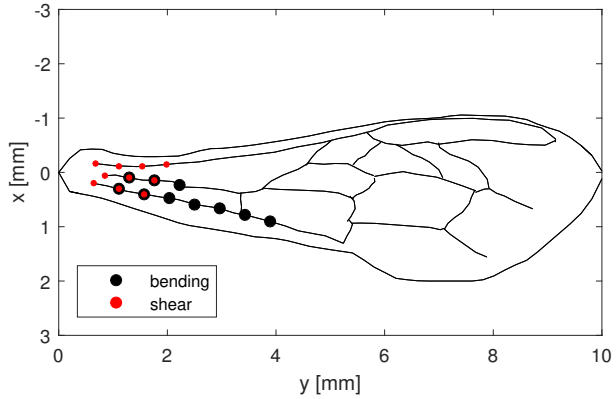

Figure 5.3: Optimal sensor placement for the honeybee *Apis mellifera*.

The campaniform sensilla of the hawkmoth and fruit fly are shown by the blue squares in Figures 5.1 and 5.2. Unfortunately, campaniform sensilla information for the honeybee was unavailable. There are differing opinions surrounding the vascular structure of the honeybee wing, and whether the hairs covering the wing have a campaniform structure. Therefore, only the hawkmoth and fruit fly results are compared to the insects' known campaniform sensilla locations. Additionally, it should be noted that the campaniform sensilla shown in this thesis represent a portion of the known sensilla. There are large bundles near the roots of the wing which were not shown to increase clarity of the images. The sensilla structure of the hawkmoth is distributed over the wing, with bundles near the root and tip of the wing. The optimization results, on the other hand, show placement is contained to the root and leading edge. This could be attributed to the values optimized using cvx. The fruit fly campaniform sensilla are bundled near the root and center of the wing. It appears the optimization results of the fruit fly sensors more closely resemble the campaniform sensilla than that of the hawkmoth. However, further research into different optimization techniques need

to be explored for a complete explanation of the campaniform sensilla structure. The next chapter will discuss the differences between the results in [2] and the hawkmoth results in Figure 5.1.

5.2 Discussion

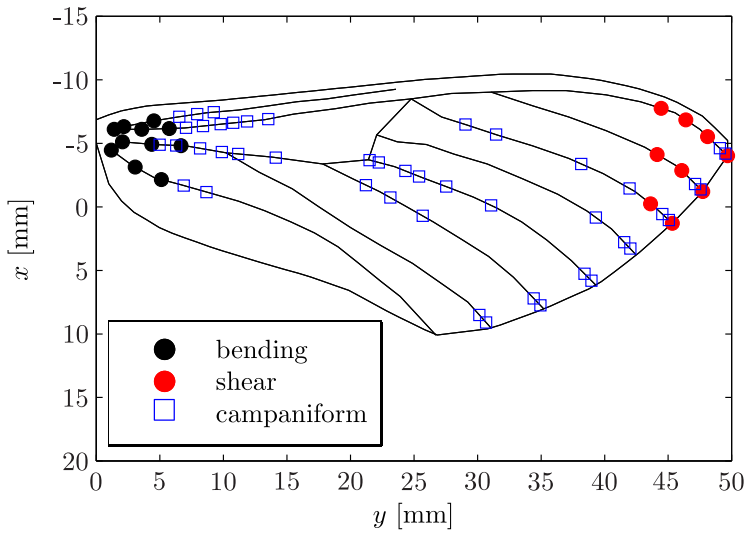

Figure 5.4: Optimal sensor placement for the hawkmoth *Manduca sexta* as shown in [2].

Comparing the results, it is evident that mode shape plays a large part in optimal sensor placement. The optimal sensor placement in [2] is shown below in Figure 5.4. Whereas the results seen in Figure 5.4 produced bending and shear sensors at the root and tip, respectively, the results using FEA analysis determined optimal placement for both bending and shear to be local to the root of the wing. Although the exact placement of the bending sensors are not identical between the two approaches, they are both bundled near the root of the wing. This is expected due to the similarities between the two bending modes used for analysis. As mentioned in Chapter 3, the bending modes were almost identical, with the large disparity seen in the first torsion

mode. In [2] the leading edge of the wing had no deflection, and therefore maximum shear information was seen near the tip at the trailing edge. From the FEA approach, we see that there is deflection along the leading edge. This corresponds to the optimal shear sensor placement of the hawkmoth beginning at the root and expanding along the leading edge towards the tip.

Chapter 6
FUTURE WORK

Further research into more accurate FEA modeling would determine how sensor placement changes based on the fidelity of the model. A study could be performed with differing levels of accuracy: modeling wing veination, using non-uniform thickness, and using non-uniform material. Flapping dynamics can also be modeled using FEA software. However, one should consider using COMSOL software as Ansys does not handle coriolis forces accurately. Additionally, measured data of the wing stroke kinematics could be attained and used in place of the models described in Chapter 4. In all cases, it is recommended to change only one variable of the analysis in order to maintain comparable results. If more than one variable is altered, it would be impossible to determine which change contributed to the final sensor placement results. This thesis develops a deeper look at insect campaniform sensilla and using biological systems as inspiration for applying distributed systems with modern control techniques. Further research could explore different optimization techniques to determine if optimizing for values other than strain produce sensor placement results which better correspond to the insects' campaniform sensilla. These values could include optimizing for strain rate in addition to strain, or for inertial rotation forces.

BIBLIOGRAPHY

[1] R. S. Steven N. Fry and M. H. Dickinson, "The aerodynamics of hovering flight in *drosophila*," *The Journal of Experimental Biology*, vol. 208, pp. 2303–2318, 2005.

[2] B. T. Hinson and K. A. Morgansen, "Gyroscopic sensing in the wings of the hawkmoth *manduca sexta*: The role of sensor location and directional sensitivity," *Bioinspiration & Biomimetics*, vol. in review, 2014.

[3] S. A. Combes and T. L. Daniel, "Flexural stiffness in insect wings," *The Journal of Experimental Biology*, vol. 206, pp. 2979–2987, 2003.

[4] J. T. Vance, D. L. Altshuler, W. B. Dickson, M. H. Dickinson, and S. P. Roberts, "Hovering flight in the honeybee *apis mellifer*: Kinematic mechanisms for varying aerodynamic forces," *Physiological and Biochemical Zoology*, vol. 87, pp. 870–881, 2014.

[5] W. B. Dickson, P. Polidoro, M. M. Tanner, and M. H. Dickinson, "A linear systems analysis of the yaw dynamics of a dynamically scaled insect model," *The Journal of Experimental Biology*, vol. 213, pp. 3047–3061, 2010.

[6] N. F. Rieger, "The relationship between finite element analysis and modal analysis," *Sound and Vibration*, vol. 20, pp. 16–18, 23–31, Jan. 1986.